

1 **Analysis of insoluble particles in hailstones in China**

2 Haifan Zhang<sup>1</sup>, Xiangyu Lin<sup>1</sup>, Qinghong Zhang<sup>1\*</sup>, Kai Bi<sup>2\*</sup>, Chan-Pang Ng<sup>1</sup>, Yangze Ren<sup>1</sup>, Huiwen Xue<sup>1</sup>, Li Chen<sup>3</sup>, Zhuolin  
3 Chang<sup>4</sup>

4 <sup>1</sup>Department of Atmospheric and Oceanic Sciences, School of Physics, Peking University, Beijing 100871, China

5 <sup>2</sup>Field Experiment Base of Cloud and Precipitation Research in North China, China Meteorological Administration, Beijing  
6 101200, China

7 <sup>3</sup>Electron Microscopy Laboratory, Peking University, Beijing 100871, China

8 <sup>4</sup>Key Laboratory for Meteorological Disaster Monitoring and Early Warning and Risk Management of Characteristic  
9 Agriculture in Arid Regions, China Meteorological Administration, Yinchuan 750002, China

10 \*Corresponding author: Qinghong Zhang ([qzhang@pku.edu.cn](mailto:qzhang@pku.edu.cn)); Kai Bi ([bikai\\_picard@vip.sina.com](mailto:bikai_picard@vip.sina.com))

11



describing the whole convective cloud, especially the deep convection in severe storms. Absence about microphysical observations of ice-nucleating particles within severe storms leads to uncertainty in understanding cold cloud process, e.g., hailstone formation, while obstructed by a lack of complete microphysical observation in clouds about ice-nucleating particles. There are two ways to sample ice-nucleating particles: The first involves an airborne instrument, named continuous flow thermal gradient diffusion chamber (Rogers et al., 2001; Prenni et al., 2009; DeMott et al., 2010). The second is done in the laboratory, where scientists conduct freezing experiments (Hoose and Möhler, 2012). In most cases, it is necessary for an aircraft to collect air parcels for measurement of the physical properties of ice-nucleating particles in the air. However, former field projects sampled air parcels in anvils of convective clouds, cirrus and winter mixed-phase stratiform clouds. No flight report or article has reported that they sampled air parcels through cores in deep convection. This phenomenon is consistent with consideration for flight security. Thus, current observation is insufficient for describing the whole convective cloud, especially the deep convection in severe storms. Absence about microphysical observations of ice-nucleating particles within severe storms leads to uncertainty in understanding cold cloud process.

Hailstones, as a product of deep convective clouds, serves as a carrier of information within these clouds. Recently, (Li et al., 2020).

Recently, detection for soluble ions along with isotopic analysis of a huge hailstone revealed an up-and-down hailstone growth trajectory, which demonstrated that the different shells were formed at different heights (Li et al., 2020). Further analysis revealed large diversity in number concentration of soluble ions among hailstones from different hailstorms (Li et al., 2018). Further, the detection of soluble ions along with isotopic analysis of a huge hailstone revealed an up-and-down hailstone growth trajectory, which demonstrated that the different shells were formed at different heights (Li et al., 2020). These studies have proved aerosol information in convective cloud may be recorded in soluble particles within hailstones (Li et al., 2020, 2018; Knight, 1981; Jouzel et al., 1975). These studies have proved that aerosol information in convective cloud may be recorded in soluble particles within hailstones (Li et al., 2018, 2020). Similarly, insoluble particles in hailstones can also record aerosol information in severe storms.

Former studies showed that species and number concentration of insoluble particles in hailstones (Vali, 1968; Rosinski, 1966; Michaud et al., 2014) would influence heterogeneous nucleation process (Hoose and Möhler, 2012) and further hailstone formation (Knight, 1981). Information on the species of insoluble particles can determine the freezing temperature when these particles participate in the initiation of ice crystal formation and subsequently impact hailstone embryo growth. Biological particles in hailstones, such as pollen and bacteria, are more efficient ice-nucleating particles than dust within the ice nucleation region of storm clouds (Michaud et al., 2014). They can raise the freezing threshold temperature above  $-15^{\circ}\text{C}$ , while dust particles are activated to form ice crystals at temperatures below  $-15^{\circ}\text{C}$  (Michaud et al., 2014). In addition to species, number concentration of insoluble particles can also influence the hailstone formation. When more dust particles were considered, a model simulation resulted in larger number concentration of ice crystals, smaller graupels (one type of hailstone embryos) size,



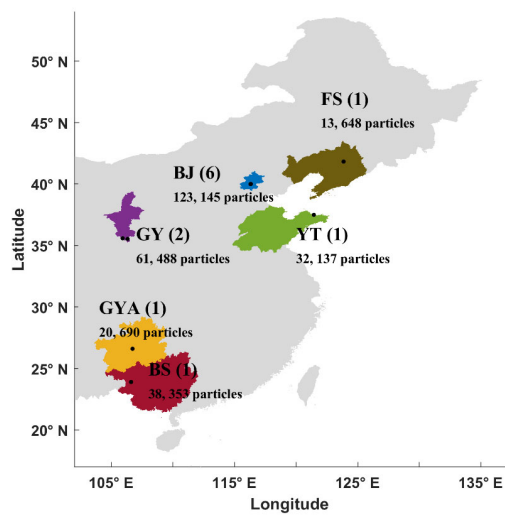
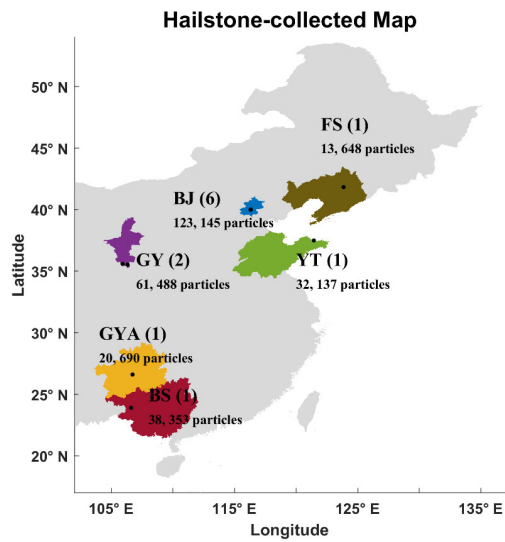


Fig. 1: Geographical distribution of hailstone-collected provinces. Black dots are hailstones. The collecting locations of hailstones are indicated by black dots. Provinces of China from which the hailstones were collected are shown in represented by six different colors. The sample abbreviations are marked in the figure with the number of hailstones sampled we analyzed was indicated in

101 parentheses. Abbreviations (corresponding to Table. 1): ~~BJ, Beijing City; GY, Guyuan City - BeiJing; BS, Baise City - BaiSe; FS,~~  
102 ~~Fushun City; YT, Yantai City - FuShun; GY - GuYuan; GYA, Guiyang City - GuiYAng; YT - YanTai.~~



<sup>a</sup> Date and ~~Beijing local solar~~ time of hailstorms occurrences. Hailstones were collected within 30 min during hail.

<sup>b</sup> ~~Hailstone collecting location.~~

<sup>c</sup> ~~Latitude and longitude where the hailstone were collected.~~

<sup>d</sup> ~~The total~~Total column water vapor values (~~Beijing local solar~~ time of ERA5 reanalysis data in square brackets (Hersbach et al., 2018)).

<sup>e</sup> Depth between freezing level ~~height~~ and orography (~~Beijing local solar~~ time of ERA5 reanalysis data in square brackets(Hersbach et al., 2018)).

<sup>f</sup> ~~Sample~~Location and ~~sample~~ abbreviations.

<sup>g</sup> Numbers of hailstones used in ~~the~~ experiments.

<sup>h</sup> Diameter of hailstone (— means no record).

<sup>i</sup> Insoluble particle number in hailstones ~~from the same province.~~

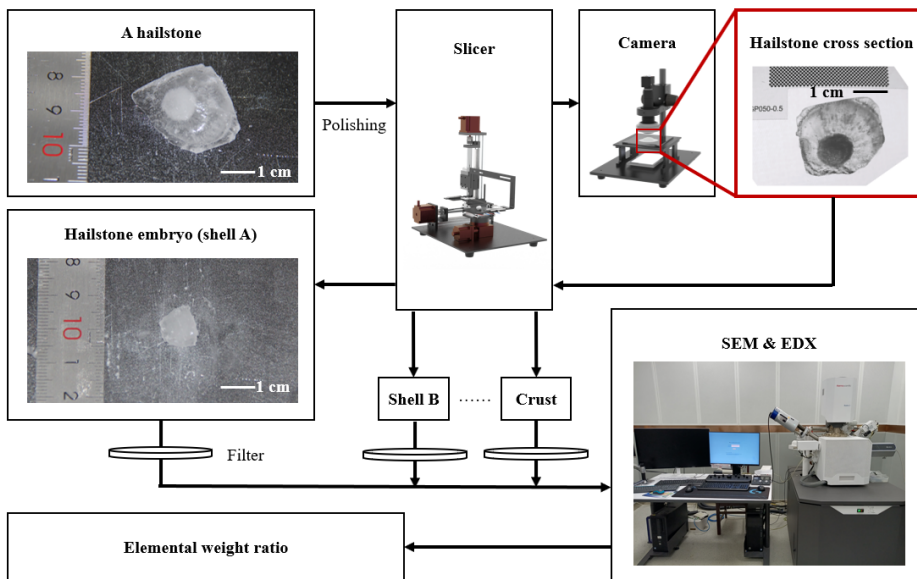
Formatted: Font: Bold

Formatted: Font: Bold

Formatted: Font: Bold



105 Insoluble particles were extracted in the experiments (Fig. 2). The surface of ~~the~~each hailstone was polished to remove  
106 any attached grass or soil. ~~Then, Subsequently, the~~ hailstones were sliced into cross-sections along the major axis,  
107 corresponding to the size of the hailstone embryo. The cross-sections were ~~further~~ sliced into ~~several~~ shells using heated Fe-  
108 Cr alloy wire at ~~an~~ air temperature below  $-8^{\circ}\text{C}$ . The shells within a hailstone were distinguished based on their natural  
109 transparency or opacity. ~~Hailstones~~However, hailstones with a major axis  $< 7$  mm could not be sliced ~~because of~~due to  
110 the mass loss ~~with~~resulting from heating using our experimental apparatus.



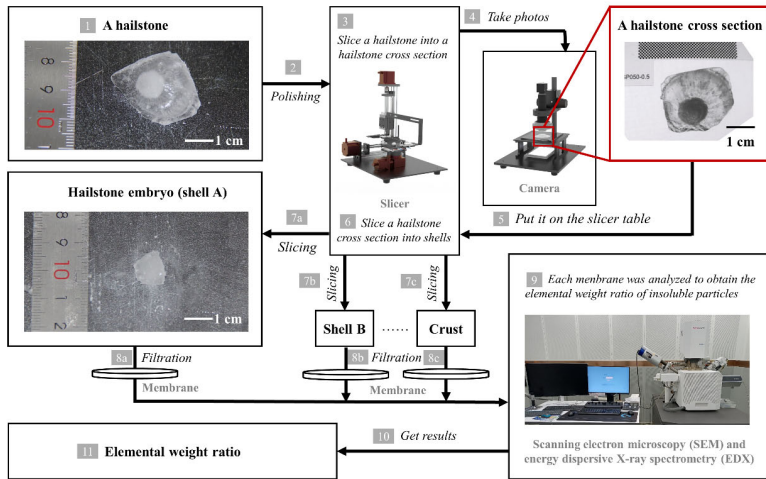


Fig. 2: Schematic diagram showing illustrating the experimental framework. [1-2] The surface of the each hailstone was polished to remove any attached grass or soil and. [3] Subsequently, the hailstones were sliced into cross-sections along the major axis. The shells within a, corresponding to the size of the hailstone embryo. [4-7] After photographing the hailstone cross-sections, they were further subdivided into shells using heated Fe-Cr alloy wire at an air temperature below  $-8^{\circ}\text{C}$ . The shells were distinguished based on their natural transparency or opacity. Solution [8] The solution of melting shell samples was then passed through a filter membrane to obtain isolate the insoluble particles. [9] Each shell sample was analyzed within about 4 hours by underwent analysis using scanning electron microscopy and energy-dispersive X-ray spectrometry to determine the elemental weight ratios of the insoluble particles within approximately 4 hours. [11] Finally, the elemental weight ratio information of hailstones was obtained.

Formatted: No widow/orphan control

The shells were sequentially labeled with capital letters in alphabetical order, starting from the inner shell to the crust. For example, the embryo of a hailstone was embryo (designated as shell A. To obtain insoluble particles,) and progressing toward the crust. After the ice shells were melted melting into a solution, and the solution was filtered through a filter membrane (VSWP01300, Merck KGaA, Germany) with a pore size of 30 nm. The filter membrane was flushed five times with The 1 mL (a total of 5 mL) of distilled water underwent five passes through the filter membrane to ensure as many maximum retention of insoluble particles as possible stuck on the filter membrane. The Subsequently, the filter membrane was dried under an air temperature of about approximately  $40^{\circ}\text{C}$  for electron microscopy to satisfy the dry-environment requirements of SEM.

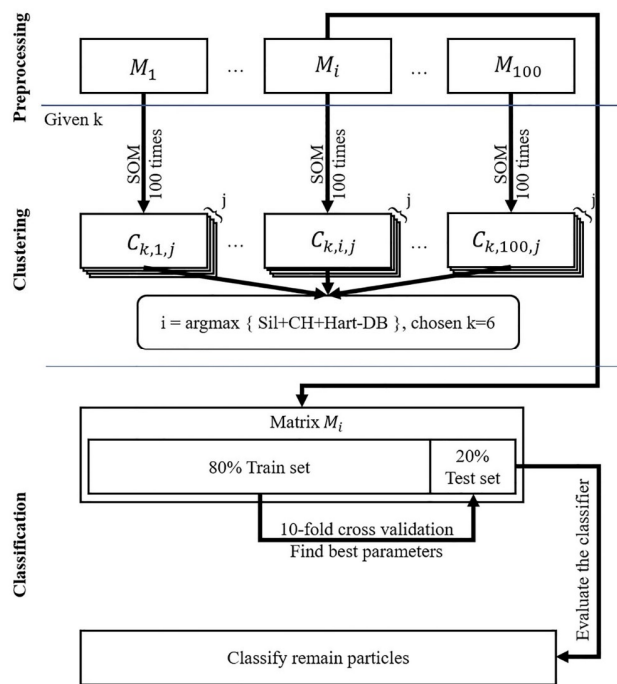
Formatted: Font: 小五, Bold

The number of insoluble particles in each shell was determined by using scanning electron microscopy (SEM), focusing with a focus on particles  $>$  larger than  $0.16\ \mu\text{m}$ . The length along the major axis of the particles was measured using

132 Aztec software (Aztec software, Oxford Instruments plc, UK) on SEM images. ~~Energy~~The software was able to randomly  
 133 ~~capture electron microscopy photos of the membrane (Aztec User Manual). No particle will be counted repeatedly. Energy-~~  
 134 dispersive X-ray spectrometry (EDX) was ~~used~~utilized to determine the elemental weight ratios of ~~the~~ particles. Only elements  
 135 with an atomic number ~~>-greater than~~ 4 could be detected ~~because~~due to the X-ray input window ~~was~~being made of beryllium.  
 136 Each shell sample was analyzed within ~~about~~approximately 4 hours by SEM and EDX. The scanning mode of SEM was set  
 137 in ~~a~~ random order to reduce ~~the error~~errors caused by bias in ~~the~~ detection area.

## 138 2.2 Clustering and classification

139 The number of insoluble particles was measured using Aztec on SEM images, but the species could not be determined  
 140 directly and were identified by machine learning ~~method~~. The criteria of species classification were established by the ~~self-~~  
 141 ~~organized maps~~SOMs method to determine the species of unclassified particles. These labeled particles were then regarded as  
 142 ~~true species and used to train a~~training set in random forest classifier. Details are presented in Fig. 3.



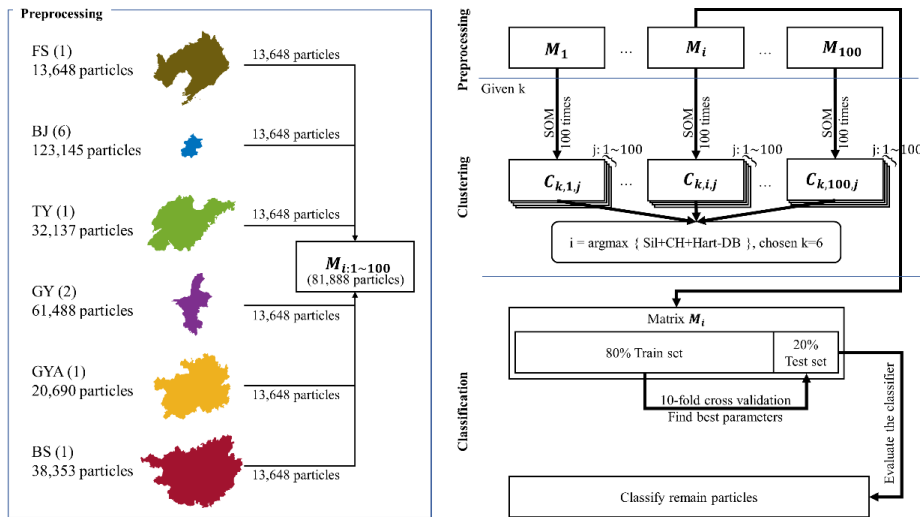


Fig. 3: Schematic diagram showing illustrating the methodological framework of the methods used for particle identification in this study. The A total of 100 matrices  $M_i$  with  $i$  ranging from 1 to 100, were used utilized in self-organized maps clustering analyses, and each of them included containing 81,888 unidentified 81,888 particles with 19 elemental features (N, Na, Mg, Al, Si, P, S, Cl, K, Ca, Ti, Cr, Mn, Fe, Ni, Cu, Br, Ba, and Pb). Centroid The centroid matrix  $C_{k,i,j}$  was represents the clustering results by obtained through the self-organized maps method with chosen a given cluster number  $k$ . The operation of self-organized maps operation with the same  $k$  was repeated 100 times to ensure the result robustness of results. The, where  $j$  is denotes the number of repeating time, repetitions ranging from 1 to 100. Four indexes, i.e., indices, Silhouette index (Sil), Calinski–Harabasz index (CH), modified Hartigan index (Hart), and Davies–Bouldin index (DB), were used employed to determine best centroid number the optimal parameters  $k$ ,  $i$ , and  $j$ . The matrix  $M_i$  containing identified 81,888 particles, was separated as randomly divided into a training set (80 %) and a test set in (20 %) for random forest classification with. The 10-fold cross-validation. The best classifier was used utilized to classify remain particles determine the best tree. Abbreviations (corresponding to Table 1): BJ - BeiJing; BS - BaiSe; FS - FuShun; GY - GuYuan; GYA - GuiYAng; YT - YanTai.

With reference to the studies of Ault et al. in 2012 and Kirpes et al. in 2018 and considering the results of elemental weight ratios determined by EDX analysis (Ault et al., 2012; Kirpes et al., 2018), 19 elements (N, Na, Mg, Al, Si, P, S, Cl, K, Ca, Ti, Cr, Mn, Fe, Ni, Cu, Br, Ba, and Pb) were selected to confirm the species of particles. C and O were not taken in account when clustering or classifying particles as the membrane filters were made from cellulose acetate and cellulose nitrate, which contain C, H, N, and O. We could not detect H because the ray input window was made of beryllium. All particles showed high contents of C and O but different contents of N, so N was retained as a feature of classification.

164  
165 With reference to the studies of Ault et al. (2012) and Kirpes et al. (2018) and considering the results of elemental weight  
166 ratios determined by EDX analysis, 19 elements (N, Na, Mg, Al, Si, P, S, Cl, K, Ca, Ti, Cr, Mn, Fe, Ni, Cu, Br, Ba, and Pb)  
167 were selected to confirm the species of particles. C and O were not taken in account when clustering or classifying particles as  
168 the membrane filters were made from cellulose acetate and cellulose nitrate, which contain C, H, N, and O. We could not detect  
169 H because the ray-input window was made of beryllium. All particles showed high contents of C and O but different contents  
170 of N, so N was retained as a feature of classification.

171 Species of aerosol particles vary regionally with sampling location (Tao et al., 2017). Therefore, when establishing the  
172 matrices of elemental weight ratios for clustering, equal amounts of data were randomly extracted from the sample data from  
173 each province to ensure the inclusion of a consistent proportion of samples from each region in the training process. A hailstone  
174 FS collected from Fushun City, Liaoning Province was shown to contain 13,648 insoluble particles, which was the smallest  
175 among all samples from six provinces (Fig. 1). With random sampling of 13,648 particles from each province, the matrix used  
176 in clustering analyses included 81,888 particles. This operation was repeated 100 times to obtain 100 matrices  $\mathbf{M}_i$  with  $i$   
177 ranging from 1 to 100.

178 Each matrix  $\mathbf{M}_i$  was clustered using the SOM method, which is an unsupervised machine learning method that  
179 represents high-dimensional data in low-dimensional space while preserving the topological structure of the data. The neuronal  
180 network was set to  $k$  neurons in a layer, where  $k$  is the given clustering center number from 2 to 10. Each SOM operation  
181 produces a centroid matrix  $C_{k,i,j}$ , where  $i$  is the number of particle sample replicates, as mentioned above, and  $j$  is the  
182 number of rounds of SOM operation. Weights of a neuron describe its position in multivariate space and can be taken as a  
183 cluster center. The operation of SOM with the same neuronal network setting was repeated 100 times to ensure the robustness  
184 of the centroid matrix  $C_{k,i,j}$ . Four indexes, i.e., Silhouette index, SOMs method. SOMs belong to the category of competitive  
185 learning algorithms and are a type of artificial neural network (Kohonen, 1990). A basic SOMs network consists of an input  
186 layer, weight vectors, and an output layer. Each neuron in the output layer possesses a set of weight vectors, which represent  
187 the topological structure of the neurons in the output layer, associated with the inputs. SOMs are commonly used as  
188 dimensionality reduction algorithms, enabling the representation of high-dimensional data in a lower-dimensional structure  
189 while preserving the original topology. When SOMs are trained on unlabeled data for clustering purpose, it proves highly  
190 beneficial in clustering unlabeled and high-dimensional inputs into visualized two-dimensional outputs.

191 We utilized the SOMs code from MATLAB's deep learning toolbox. The input of SOMs is  $\mathbf{M}_i$ . At begin, the neural  
192 network in the output layer was initialized as 1-D dimension with  $k$  neurons. The number of neurons in the output layer  
193 matches  $k$  ranging from 2 to 10. The operation of SOMs with the same initialized  $k$  neurons and input matrix  $\mathbf{M}_i$  was  
194 repeated 100 times to ensure result robustness. The clustering result was stored in matrix  $C_{k,i,j}$ , which corresponded to the

Formatted: Font: 五号

Formatted: Don't add space between paragraphs of the same style

Formatted: Don't add space between paragraphs of the same style

195 given  $k$  centroids in  $\mathbf{M}_i$  with  $j^{\text{th}}$  SOMs operation. Each  $\mathbf{C}_{k,i,j}$  matrix consists of  $k$  rows and 19 columns (corresponding  
 196 to the number of elemental features). Four indices, namely, the Silhouette index (Rousseeuw, 1987), the Calinski–Harabasz  
 197 index (Calinski and Harabasz, 1974), the modified Hartigan index (Sibson and Hartigan, 1976), and the Davies–Bouldin index  
 198 (Davies and Bouldin, 1979), were selected as evaluation indicators to determine the parameters  $k$ ,  $i$  and  $j$ . The best  $k$ ,  $i$   
 199 and  $j$  was chosen by combining the evaluation of the four indexes (Fig. 4) and elemental weight ratios of each centroid. The  
 200 Silhouette index, Davies–Bouldin index, and Calinski–Harabasz index assess the similarity between a particle and others  
 201 within the same cluster, as well as the dissimilarity across different clusters for a given  $k$ . Hartigan index evaluates whether it  
 202 is worthy to increase the  $k$ . Notably, Hartigan index has undergone modifications that preserve its statistical meaning while  
 203 conserving computational resources.

204 Hartigan index (Sibson and Hartigan, 1976) is defined as:

$$205 \quad H(k) = (N - k - 1) \left[ \frac{err(k)}{err(k+1)} - 1 \right], k = 2 \sim 10 \quad (1)$$

$$206 \quad err(k) = \sum_{g=1}^k \sum_{x_g \in C_g} (x_g - C_g)^2 \quad (2)$$

207  
 208  $k$  : the number of clusters.

209  $C$  : the centroid of all data

210  $N$  : the number of observations in data

211  $C_g$  : the centroid of cluster  $g$

212  $x_g$  : the observation of cluster  $g$

213  $x_n$  : the observation of data

214 The calculation of  $H(k)$  requires clustering for values of  $k$  ranging from 2 to 11 in order to obtain  $H(2)$ ,  $H(3)$ , ...,  
 215  $H(10)$ . Clustering particles into 11 clusters would require performing an additional 10,000 iterations of the SOMs, with 100  
 216 iterations of extracting  $\mathbf{M}_i$  and 100 iterations of SOMs for each  $\mathbf{M}_i$ . Additionally, we observed that the SOMs did not perform  
 217 well in the Silhouette index (Sil), the Calinski–Harabasz index (CH), and the Davies–Bouldin index (DB) when  $k = 2$ . As a  
 218 result, we introduced modifications to the Hartigan index.

$$219 \quad Hart(k) = [N - (k - 1) - 1] \left[ \frac{err(k-1)}{err(k)} - 1 \right], k = 2 \sim 10 \quad (3)$$

$$220 \quad err(k) = \sum_{g=1}^k \sum_{x \in C_g} (x_g - C_g)^2, k \geq 2 \quad (4)$$

221  
 222 When  $k = 1$ , it indicates that all particles are belong to one cluster.

$$err(1) = \sum_{n=1}^N (x_n - C)^2 \quad (5)$$

In clustering with a specific value of  $k$ , our objective is to have particles tightly grouped together in feature space while ensuring that the centroids exhibit a significant dispersion compared to  $k - 1$ . A higher value of  $Hart(k)$  for a given  $k$  indicates improved clustering performance. The best  $k$ ,  $i$  and  $j$  was chosen by combining the evaluation of the four indices (Fig. 4). We applied max normalization to rescale the four indices,  $Sil(k)$ ,  $CH(k)$ ,  $DB(k)$ , and  $Hart(k)$ . Subsequently, the best combination of  $k$ ,  $i$  and  $j$  was determined, resulting in  $\{Sil(k, i, j) + CH(k, i, j) + Hart(k, i, j) - DB(k, i, j)\}$  reaching its maximum.

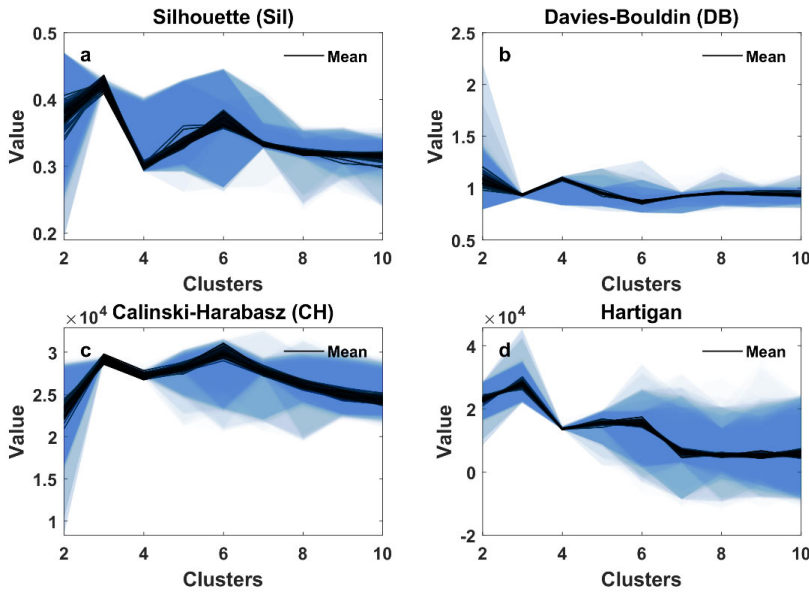


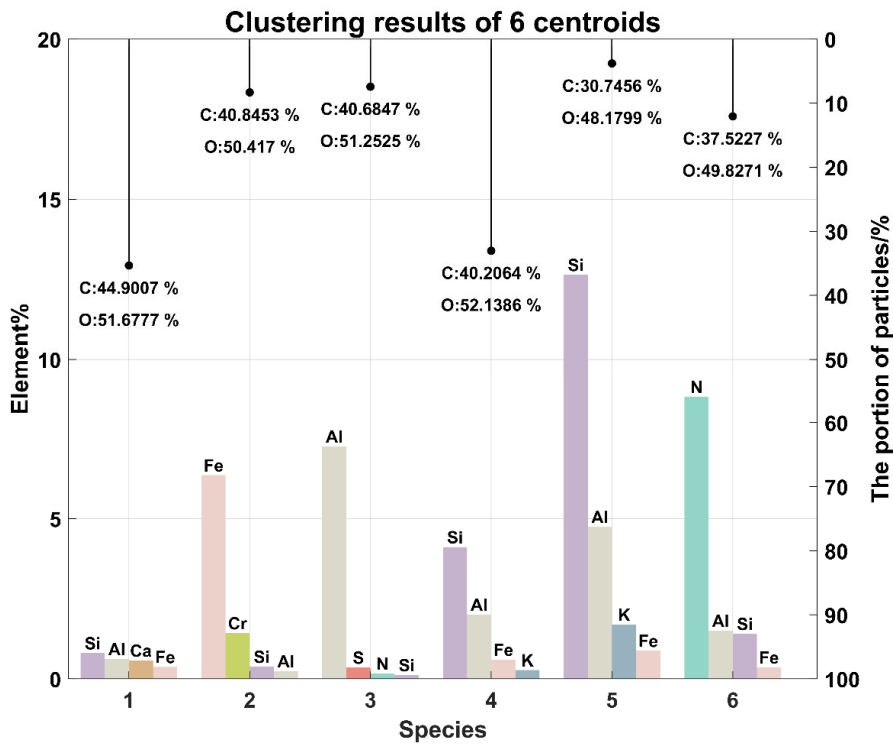
Fig. 4: Evaluation of self-organized maps clustering results. The clustering results of self-organized maps clustering results by were evaluated using (a) Silhouette index, (b) Davies-Bouldin index, (c) Calinski-Harabasz index, and (d) Hartigan index. The self-organized maps operation was repeated 100 times to obtain each randomly sampled matrix  $M_i$ , ensure result robustness.

The solid lines and shading represent the average and spread of 100 repetitions, respectively.

The centroid matrix  $C_{k,i,j}$  with best  $k$ ,  $i$  and  $j$  was treated as a training set for random forest classification. The chosen centroid matrix  $C_{k,i,j}$  with the top four elements is shown in Fig. 5 with  $k = 6$ . The first species with low elemental weight ratio except C and O contents was considered to be organics. The second species with high Fe content and low Cr

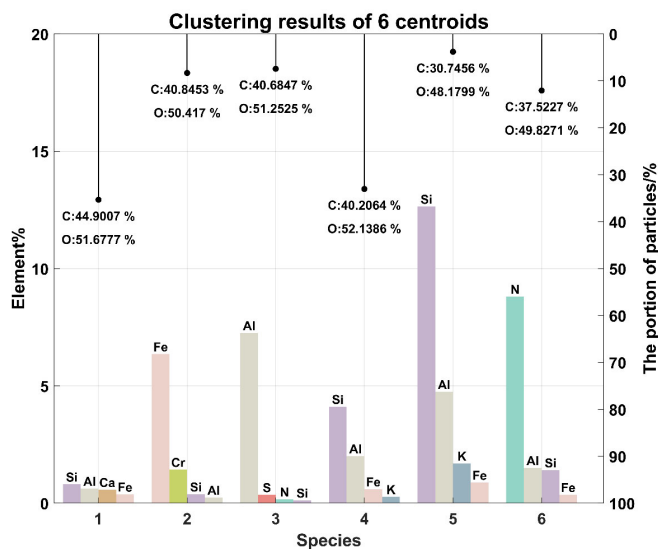
Formatted: Indent: First line: 0.74 cm

240 content was introduced by the material of the slicer used in the experiment. The third species had a high Al content representing  
 241 oxides or carbonates of aluminum. The fourth and fifth species were mineral silicates. So that, the third, fourth, and fifth  
 242 species were referred to as "dust". The last species with high N content was protein-containing biological aerosol.



243





244

245 Fig. 5: Centroids of clustering with six clusters from self-organized maps results and each species portion. Colored bars show the  
 246 top four elements of each species. The stem bars show the portion of each species. The average contents of C and O of each species  
 247 are marked at the end of the stem bars.

248

249 The random forest method was applied in classifying insoluble particles, which involves randomly growing 100  
 250 classification trees. The training set consisted of 80% of  $M_1$  and 10-fold stratified cross-validation was applied during the  
 251 training process to find the best tree among the 100 random trees. The remaining 20% particles of  $M_1$  was used as the test  
 252 set to evaluate the classifier. The best classification tree and the confusion matrix of the evaluation of testing classification  
 253 results are shown in Fig. 6. All remaining insoluble particles were classified by this tree. Finally, results we identified three  
 254 species: organics, dust, and bioprotein aerosols.

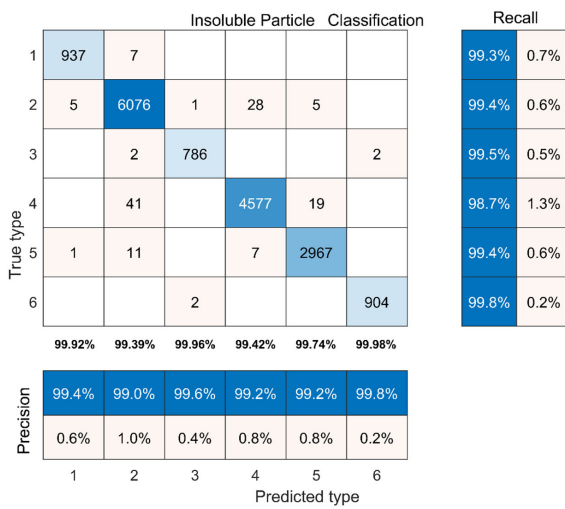
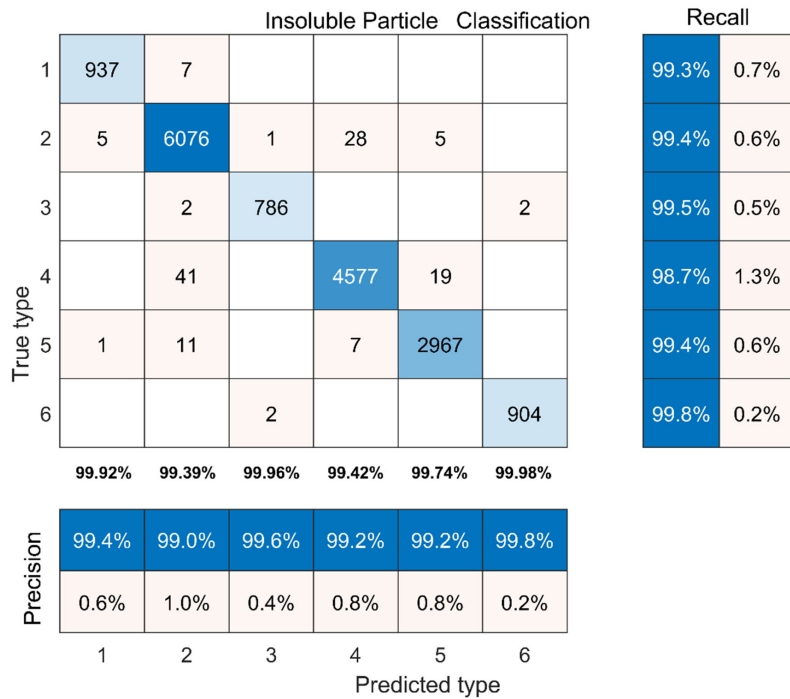


Fig. 6: Confusion matrix of the best random forest classifier tree. The numbers on the diagonal are accurately predicted insoluble particles. Numbers in bold indicate the accuracy of prediction of each type.

### 2.3 Calculation of insoluble particles number concentration

Particle number was converted to a number concentration as follows per cubic centimeter volume water (hereinafter referred to as number concentration) using the following formula:

$$n_{liquid} \cdot V_{liquid} = N_{liquid} = N_{diluted} = n_{diluted} \cdot V_{diluted} \quad (1)$$

Part of the solution was not consumed in these experiments and was retained as a backup. During several experiments, the melted shell solution was diluted.

$$n_{diluted} = n_{used} = \frac{N_{used}}{V_{used}} = \frac{N_{filter}}{V_{used}} \quad (2)$$

SEM can provide the number of particles on a filter, but the whole area of the filter cannot be scanned. We assumed

$$n_{liquid} \cdot V_{liquid} = N_{liquid} = N_{diluted} = n_{diluted} \cdot V_{diluted} \quad (6)$$

The number of insoluble particles in the melted shell solution ( $N_{liquid}$ ) can be calculated by multiplying their number concentration ( $n_{liquid}$ ) with the volume of the shell solution ( $V_{liquid}$ ). Part of the solution was not used up in the experiments and was kept as a backup. Therefore, the shell solution was diluted in some experiments and part of the solution was consumed in the experiments. As in the melting solution, the number of insoluble particles in the diluted solution ( $N_{diluted}$ ) can be calculated by multiplying their number concentration ( $n_{diluted}$ ) with the volume of the diluted solution ( $V_{diluted}$ ). The total particle number in the melted shell ( $N_{liquid}$ ) remains unchanged during the dilution process ( $N_{diluted}$ ).

$$n_{diluted} = n_{used} = \frac{N_{used}}{V_{used}} \quad (7)$$

The number concentration of the diluted solution ( $n_{diluted}$ ) is equal to that of the consuming part ( $n_{used}$ ). Assuming the rinsing operation ensures all insoluble particles in the shell were uniformly distributed on the filter and the scanning mode of SEM was set as "random scanning". A such relationship between membrane, the number of scanned insoluble particles and the number of particles on the filter:

$$\frac{S_{filter}}{S_{images}} = \frac{N_{filter}}{N_{count}} \quad (3)$$

In the above formulas,  $n$  is the number concentration of insoluble particles;  $N$  in the consumed solution ( $N_{used}$ ) is the number of insoluble particles;  $V$  is the volume of the solution;  $S$  is the area of the filter; subscript *liquid* refers to the melted shell; subscript *diluted* refers to the diluted solution; subscript *used* refersequal to the consumed diluting solution; subscript *filter* refers to the filter membrane;  $N_{count}$  is the number of number of insoluble particles counted on the filter; and  $S_{images}$  is the area of the microseopic image membrane ( $N_{filter}$ ).

We use SEM to capture electron microscopy images of the membrane. Assuming a uniform distribution of insoluble particles on the filter membrane, a software randomly capture electron microscopy photos of the membrane and count the visible insoluble particles in those images. The relationship between total number of visible insoluble particles counted in the images ( $N_{count}$ ) and  $N_{filter}$  is:

$$\frac{S_{images}}{S_{filter}} = \frac{N_{count}}{N_{filter}} \quad (8)$$

That is,  $N_{filter}$  is determined by multiplying  $N_{count}$  by the ratio of the areas between the entire filter membrane ( $S_{filter}$ ) and the electron microscopy images ( $S_{images}$ ). These three formulas Eq. (6-8) were reduced to Eq. (4):

$$n_{liquid} = \frac{1}{V_{liquid}} \cdot \frac{S_{filter}}{S_{images}} \cdot \frac{V_{diluted}}{V_{used}} \cdot N_{count} \quad (4)$$

where

$$n_{liquid} = \frac{1}{V_{liquid}} \cdot \frac{S_{filter}}{S_{images}} \cdot \frac{V_{diluted}}{V_{used}} \cdot N_{count} \quad (9)$$

Here,  $S_{filter}$ ,  $S_{images}$ ,  $N_{count}$ ,  $V_{diluted}$ , and  $V_{used}$  can be measured. The liquid volume ( $V_{liquid}$ ) was determined as the mean average of readings obtained by two experimenters from the test tube calibration. From Eq. (4), a tiny change in  $n_{liquid}$  can be expressed as  $dn_{liquid}$ . Take the logarithm on both sides:

$$dn_{liquid} = n_{liquid} \cdot \left( \frac{dV_{liquid}}{V_{liquid}} + \frac{dV_{diluted}}{V_{diluted}} - \frac{dV_{used}}{V_{used}} + \frac{dN_{count}}{N_{count}} \right) \quad (5)$$

$$\ln n_{liquid} = -\ln V_{liquid} + \ln S_{filter} - \ln S_{images} + \ln V_{diluted} - \ln V_{used} + \ln N_{count} \quad (10)$$

Based on Eq. (10), a tiny change in  $n_{liquid}$  can be represented as  $dn_{liquid}$ :

$$dn_{liquid} = n_{liquid} \cdot \left( -\frac{dV_{liquid}}{V_{liquid}} + \frac{dV_{diluted}}{V_{diluted}} - \frac{dV_{used}}{V_{used}} + \frac{dN_{count}}{N_{count}} \right) \quad (11)$$

As,

$$dS_{filter} = dS_{images} = 0 \quad (6)$$

The uncertainty comes from the measurement error of the experimental instruments.

$$\Delta |dn_{liquid}| \leq n_{liquid} \cdot \sqrt{\left(\frac{dV_{liquid}}{V_{liquid}}\right)^2 + \left(\frac{dV_{diluted}}{V_{diluted}}\right)^2 + \left(\frac{dV_{used}}{V_{used}}\right)^2 + \left(\frac{dN_{count}}{N_{count}}\right)^2} \quad (7)$$

So,

$$\Delta_{max} = n_{liquid} \cdot \sqrt{\left(\frac{dV_{liquid}}{V_{liquid}}\right)^2 + \left(\frac{dV_{diluted}}{V_{diluted}}\right)^2 + \left(\frac{dV_{used}}{V_{used}}\right)^2 + \left(\frac{dPs}{Ps}\right)^2} \quad (8)$$

$$dS_{filter} = dS_{images} = 0 \quad (12)$$

The uncertainty ( $\Delta$ ) of  $n_{liquid}$  comes from the measurement error of the experimental instruments, following below (Taylor, 1997):

$$\Delta = n_{liquid} \cdot \sqrt{\left(\frac{dV_{liquid}}{V_{liquid}}\right)^2 + \left(\frac{dV_{diluted}}{V_{diluted}}\right)^2 + \left(\frac{dV_{used}}{V_{used}}\right)^2 + \left(\frac{dN_{count}}{N_{count}}\right)^2} \quad (13)$$

Here, the minimum scale accuracy of the test tube containing melting solution is 0.1 mL and. The term  $dV$  represents the greatest reading error caused by human and was set to 0.05 mL. The quantity  $\frac{dN_{count}}{N_{count}}$  represents corresponds to the uncertainty of detecting associated with size of insoluble particles, which is related to and the scan settings.

$$\frac{dN_{count}}{N_{count}} = \frac{dPs}{Ps} = \frac{3}{6,340,608} \quad (9)$$

$$\frac{dN_{count}}{N_{count}} = \frac{dPs}{Ps} = \frac{3}{6,340,608} \quad (14)$$

The term  $dPs$  represents the minimum number of pixels that can be detected in an image.  $Ps$  denotes the total number of pixels in the micrograph.

## 2.4 Curves fitting

We aggregated our data insoluble particles into 0.2- $\mu\text{m}$  intervals (e.g., particle number concentration at  $D = 0.3 \mu\text{m}$ , corresponding to the sum of particles of diameter 0.2–0.4  $\mu\text{m}$  0.2  $\mu\text{m}$  bin interval in Fig. 7 and Fig. 10, and 2  $\mu\text{m}$  bin interval in Fig. 8 and Fig. 9) to fit the logarithmic normal distribution,

$$n(\ln D) = \frac{N}{\sqrt{2\pi} \ln \sigma_g} \exp \left[ -\frac{(\ln D - \ln \mu_g)^2}{2 \ln^2 \sigma_g} \right] \quad (10)$$

$$n(D) = \frac{1}{D} \cdot n(\ln D) \quad (11)$$

Here,

$$n(\ln D) = \frac{N}{\sqrt{2\pi} \ln \sigma_g} \cdot \exp \left[ -\frac{(\ln D - \ln \mu_g)^2}{2 \ln^2 \sigma_g} \right] \quad (15)$$

$N$  denotes the total number concentration of particles. Both  $n(\ln D)$  and  $n(D)$  represent the size distributions of particles, where  $D$  is the diameter of insoluble particles, and  $N$  is the total number concentration of particles. According to the above, when  $n(\ln D)$  and  $n(D)$  can be converted to each other by  $D$ .

$$n(D) = \frac{1}{D} \cdot n(\ln D) \quad (16)$$

When the  $N_{count}$  in an interval equals 1, the number concentration will show exhibit a flat tail because of due to the conversion to obtain  $n_{liquid}$ . The fitting data were selected with intervals equals to 0.2  $\mu\text{m}$  0.2  $\mu\text{m}$ . The least squares method was applied to determine the fitting parameters and  $R^2$  was used to estimate fitting parameters the goodness of fit. The two centroids of fitting parameters of organics and dust were determined by K-means method.

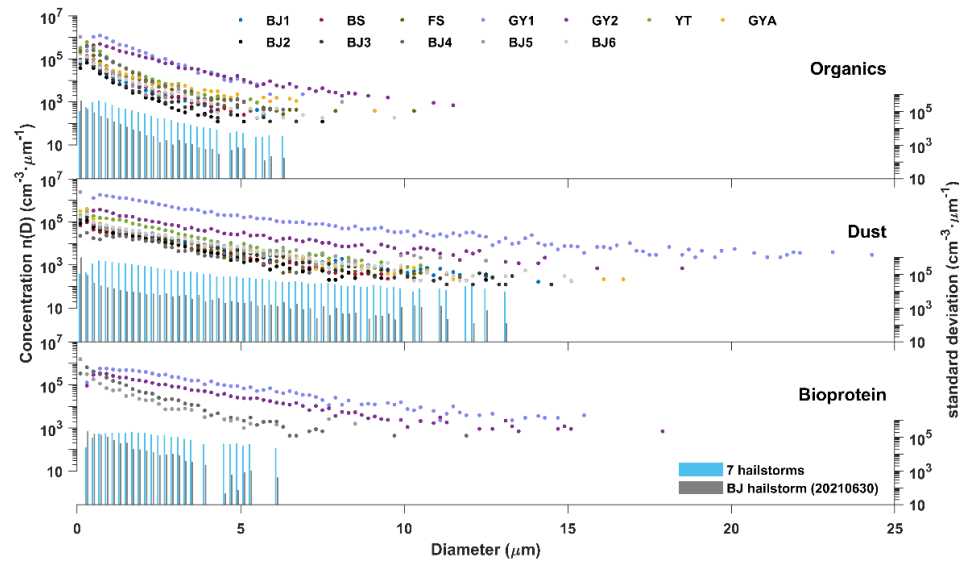
## 3 Results

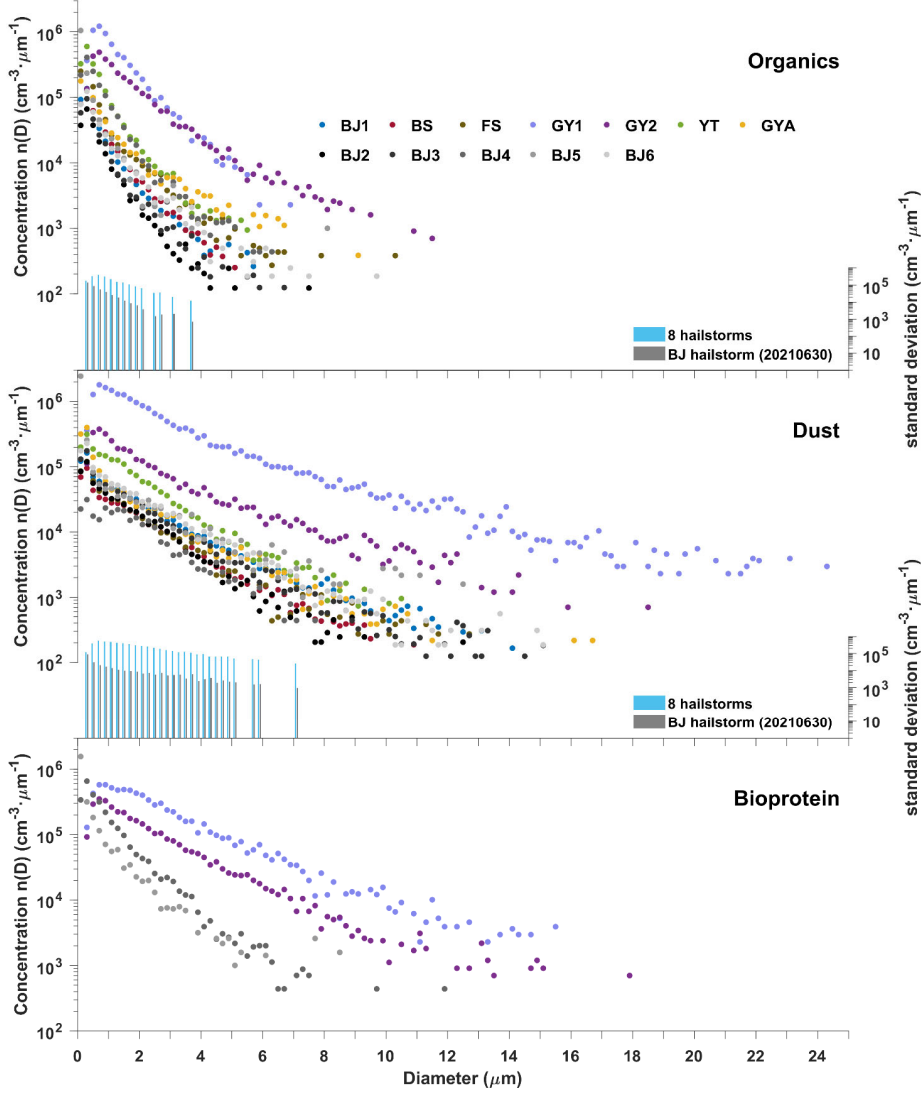
Total A total of 289,461 insoluble particles were detected from 30 shells of 12 hailstones were detected by scanning electron microscopy. Elemental weight ratios of each particle were determined using energy dispersive X-ray spectrometry. More details regarding calculating number concentration SEM. The identification of insoluble particles per cubic centimeter volume water (hereinafter referred to as number concentration) from number of insoluble particles were showed in method description. Identification of insoluble particles used self-organized map employed SOMs for clustering and random forest for

classification. Four indices were selected to determine the appropriate parameters for clustering. The clustering results ( $C_{k,i,j}$ ) were set as divided into a training and a testing set for classification. The confusion matrix of the best classifier showed that the accuracy, precision, and recall were of 99.7%, 99.4%, and 99.5%, respectively. All particles were identified and classified as organics, dust, and bioprotein aerosols (i.e., the fraction of biological aerosols with protein content).

### 3.1 Sample representativeness similarity

Five of the 12 hailstones (BJ2–BJ6) were from the same hailstorm that occurred in Beijing on June 30, 2021. The insoluble particles present in these hailstones BJ2–BJ6 showed similarity in the size distribution of organics, dust, and bioprotein aerosols but differed, while those from other 7 hailstones that from other hailstorms (BJ1, BJ2, BS, FS, GY1, GY2, YT and GYA) exhibited a wider dispersion (Fig. 7). The results were similar to those of Li et al., who reported that the number concentrations of water-soluble ions varied among hailstorm events but showed similarity in the same storm (Li et al., 2018). These analyses suggested that insoluble particles in the hailstorm may come from local natural or anthropogenic emissions (e.g., soil dust, aerosols from biomass and fossil fuel combustion, products of the conversion of gaseous precursors), which is also suggested by the results on water-soluble ions (Beal et al., 2022). The updraft within the hailstorm is likely to bring insoluble particles from local surfaces or boundary layers into deep convective clouds, as hailstorms are among the most severe storms with strong updrafts (Battaglia et al., 2022). BJ2 was selected to represent five hailstones from the same hailstorm in further analysis to simplify comparison.





861

862 **Fig. 7: Size distribution of organics, dust, and bioprotein aerosols of insoluble particles in 12 hailstones. Each number concentration**  
 863 **at diameter  $D$  – total number concentration of insoluble particles with diameter ranging**  
 864  **$0.1 \mu\text{m}$  to  $D + 0.1 \mu\text{m}$ . Colored dots refer to seven hailstones (BJ1, BS, FS, BJ1, GY1, GY2, YT, NX-1, NX-2, GY, and BS)GYA**  
 865 **which were from seven different hailstorms. Black and gray dots refer to five data from hailstones (BJ2–BJ**  
 866 **6)BJ2 to BJ6) that were from the same hailstorm that occurred recurring in Beijing on June 30, 2021. Blue and gray bars**

Formatted: Heading 1, Justified, Line spacing: single

show indicate the standard deviation of number concentration of insoluble particles from seven hailstorms and one hailstorm hailstones (BJ1, BJ2, BS, FS, GY1, GY2, YT and GYA) from 8 cases and 5 hailstones (BJ2 to BJ6) from one case, respectively. Abbreviations (corresponding to Table 1): BJ, Beijing City; GY, Guyuan City - Beijing; BS, Baise City - BaiSe; FS, Fushun City; YT, Yantai City - FuShun; GY - GuYuan; GYA, Guiyang City - GuiYAng; YT - YanTai.

### 3.2 Size distribution in embryos

All hailstone embryos analyzed in this study were graupels are graupel particles, which grows from the initial ice particles through accretion of supercooled droplets (Knight, 1981). These initial ice particles are formed through nucleation of insoluble particles where heterogeneous nucleation take place (Lamb and Verlinde, 2011). In other words, insoluble particles in graupels influence the formation of ice crystals and subsequently affect the formation of hailstone embryos.

Formatted: Space Before: 0 pt, After: 0 pt, Line spacing: 1.5 lines

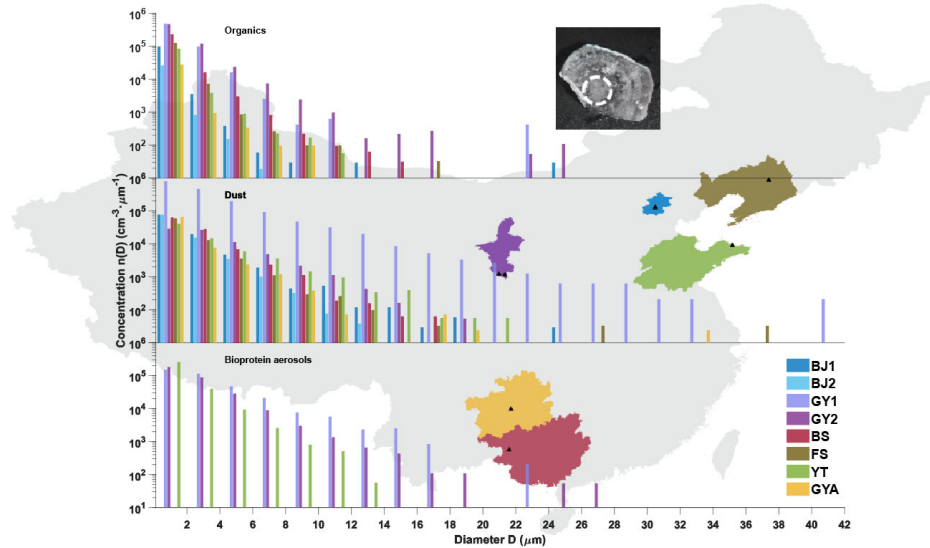


Fig. 8: Size distribution of insoluble particles in hailstone embryos. Different colors represent the provinces in China from which the hailstones were collected. Black triangles indicate the locations of hailstone sample collection. The white dashed circle highlights part of the hailstone embryo. Abbreviations (corresponding to Table 1): BJ - Beijing; BS - BaiSe; FS - FuShun; GY - GuYuan; GYA - GuiYAng; YT - YanTai.

The variations in number concentrations of dust and bioprotein insoluble particles indicate that particle number concentrations decrease exponentially with particle diameter, with markble variation observed among hailstorms (Fig. 8). BJ2 was selected to represent five hailstones from the same storm to simplify comparison. The size distribution distinguishes organics from dust and bioprotein aerosols. The number concentrations of organics from all samples decrease with particle



387 diameter less than 8  $\mu\text{m}$ , while those of GY1 and GY2 fluctuate starting at diameters of 8  $\mu\text{m}$  and 12  $\mu\text{m}$ , respectively.  
388 Compared to other hailstones, GY1 and GY2 were collected in remote areas, where is fields of rural areas dedicated to growing  
389 crops near the south of the Gobi Desert. Therefore, GY1 and GY2 have a coarse mode of organics with particle diameters  
390 larger than 12  $\mu\text{m}$ , possibly might due to the emission of spring-wheat straw burning and unrestricted diesel engine vehicles.  
391 The transport of coal combustion in surrounding cities may also contribute to the coarse mode organics. Among all cases, there  
392 is a significant variance in the size distribution of both organics and dust. The number concentration of organics from a  
393 hailstone embryo varied from 1 to 390 times, compared to those at the same particle diameter in hailstone embryos from  
394 different cases. The number concentration of dust from a hailstone embryo varied from 1 to 527 times, compared to those at  
395 the same particle diameter in hailstone embryos from different cases. The number concentrations of dust from BJ1, BJ2, and  
396 GY1 are at least 3 times higher than organics in particles of the same diameter in the range of 2–24  $\mu\text{m}$ .

397 Moreover, dust showed a wider size distribution than organics and bioproteins among all samples. Dust from GY1 had a  
398 higher number concentration and larger maximum size (42  $\mu\text{m}$ ) compared to other hailstone embryos. Hailstone samples with  
399 high insoluble particle content, i.e., GY1 and GY2, showed significantly lower total column water vapor values and smaller  
400 depth between freezing level height and orography within one hour before hailstorm occurrence, compared to other hailstones  
401 (Table 1). The competition of condensation and relative shorter updraft pathway might be responsible for the high number  
402 concentrations of organics, dust, and bioproteins in GY1 and GY2, as compared with other hailstones. Bioprotein aerosols,  
403 with high freezing efficiency, may have formed initial ice particles in GY1, GY2, and YT, while dust or organics formed initial  
404 ice particle in hailstorms in the other five cases. All hailstone embryos contained organics and dust, but not all hailstone  
405 embryos contained a significant amount of bioprotein aerosols. Due to limited comprehension of the transportation and  
406 transformation processes of biological materials, it is challenging that to establish a definitive relationship between biological  
407 protein particles and biological aerosols (Fröhlich-Nowojsky et al., 2016).

### 408 **3.3 Size distribution in shells**

409 Size distribution of each species varied little in characteristics between outer shells with the embryos (Fig. 9). In a four-  
410 shell hailstone, the number concentrations of insoluble particles exhibited V-shaped distributions (BS and YT) or inverse V-  
411 shaped distributions (BJ1) from embryo to crust. Five of nine two-shell hailstones showed higher number concentrations of  
412 dust in crusts than embryos, while seven of them showed higher number concentrations of organics in embryos than crusts.  
413 These initial ice particles are likely formed by insoluble particles where heterogeneous nucleation processes. Moreover, the  
414 quantification of differences in number concentration varied little among shells. The 90.5 % points showed that differences in  
415 number concentration of the same kind particles in a shell compared to the previous shell at the same diameter was within  
416 twice (294 data points in Fig. 9). This observation is attributed to the fact that the growth of hailstones beyond the embryo  
417 stage relies on the accretion of supercooled water rather than ice crystals (Lamb and Verlinde, 2011). That is, consequently,

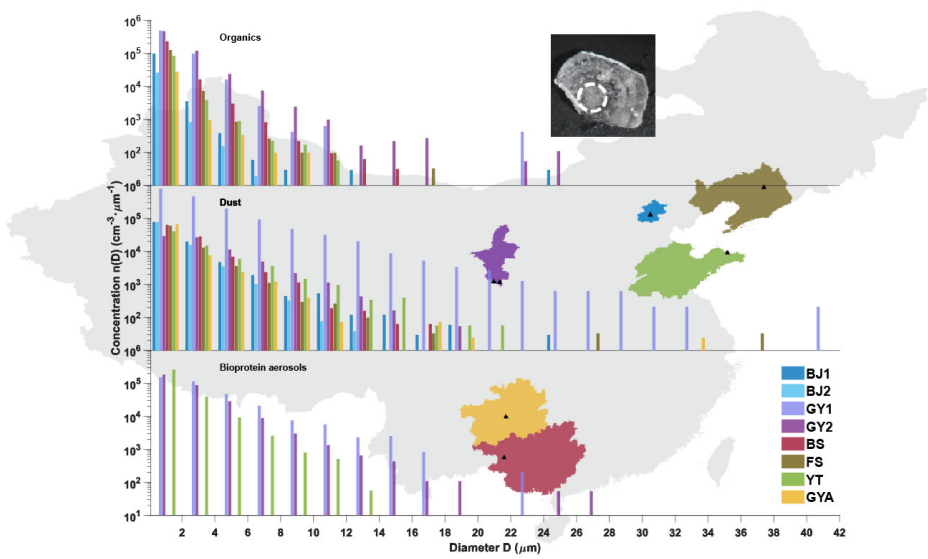
Formatted: Normal (Web), Justified, Adjust space between Latin and Asian text, Adjust space between Asian text and numbers

Formatted

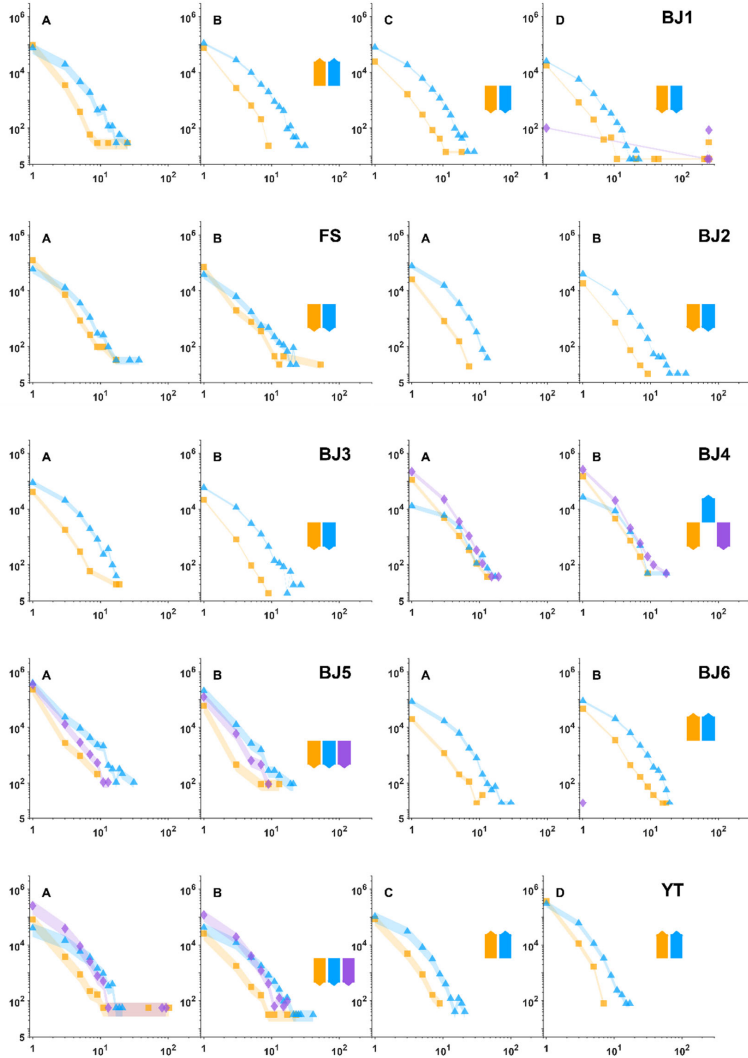
Formatted

418 the hailstone recorded not only insoluble particles in graupels possibly affected during the embryo formation of ice crystals and  
 419 subsequently affected, but also insoluble particle in the formation of hailstone embryos. The growth zone throughout the  
 420 hailstorm. As a result, the size distribution distribution of particles within the entire hailstones may represent the distribution  
 421 of insoluble particles in eight hailstone embryos (BJ1, BJ2, GY1, GY2, BS, FS, YT, and GYA) were shown in Fig. 8. deep  
 422 convection regions where the hailstones went through.

- Formatted
- Formatted
- Formatted
- Formatted
- Formatted
- Formatted
- Formatted



423



424  
 425 Fig. 8:9a, Size distribution of insoluble particles in hailstone embryos. Provinces of China, from which the hailstones were collected,  
 426 are shown in different colors. Black triangles indicate the locations of hailstone sample collection. The white dashed circle shows  
 427 part of the hailstone embryo. Abbreviations (corresponding to Table. 1): BJ, Beijing City; GY, Guyuan City; BS, Baise City; FS,  
 428 Fushun City; YT, Yantai City; GYA, Guiyang City.

Formatted: Font: +Body (等线), Not Bold

Formatted: Font: +Body (等线), Not Bold

Formatted: Font: +Body (等线), Not Bold

429  
 430 As mentioned above, BJ2 represented BJ2–BJ6. The variations in number concentrations of dust and bioprotein insoluble

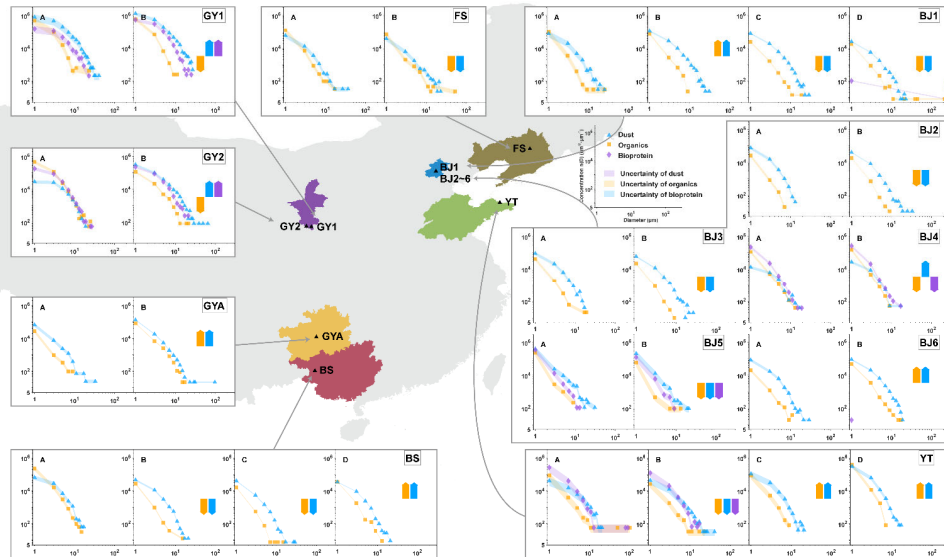
431 particles indicated that particle number concentrations decreased exponentially with particle diameter, with marked variation  
432 observed among hailstorms. The distribution distinguished organics from dust and bioprotein aerosols as the number  
433 concentrations of organics from all samples decreased with particle diameter before 8  $\mu\text{m}$ , while those of GY1 and GY2  
434 fluctuated starting at diameters of 8  $\mu\text{m}$  and 12  $\mu\text{m}$ , respectively. This was likely due to some uncontrolled residential and  
435 industrial coal burning in GY (Guyuan City). A great variance existed in size distribution of both organics and dust. The number  
436 concentrations of organics from a hailstone embryo were 1 to 390 times to those from different hailstone embryos at the same  
437 diameter. The number concentrations of dust from a hailstone embryo were 1 to 527 times to those from different hailstone  
438 embryos at the same diameter. The number concentrations of dust from BJ1, BJ2, and GY1 were at least 3 times higher than  
439 organics in particles of the same diameter in the range of 2–24  $\mu\text{m}$ . Moreover, dust showed a wider size distribution than  
440 organics and bioproteins among all samples, since dust from GY1 had a higher number concentration and larger maximum  
441 size (42  $\mu\text{m}$ ) than from other hailstone embryos. Bioprotein aerosols, with high freezing efficiency, may have formed initial  
442 ice particles in GY1, GY2, and YT, while dust or organics caused initial ice particle formation in hailstorms in cases lacking  
443 bioprotein aerosols. All hailstone embryos contained organics and dust, but not all hailstone embryos contained a significant  
444 amount of bioprotein aerosols. There were uncertainties in quantification of biological aerosols, due to poor understanding of  
445 biological transport and transformation processes (Fröhlich Nowojsky et al., 2016).

### 446 3.3 Variation in hailstone shells

447 Size distribution of each species differed little in characteristics in outer shells with the embryos (Fig. 9). For a four-shell  
448 hailstone, the number concentrations of insoluble particles showed V-shaped (BS and YT) or inverse V-shaped (BJ1)  
449 distributions from embryo to crust. Five of nine two-shell hailstones showed higher number concentrations of dust in crusts  
450 than embryos, while seven of them showed higher number concentrations of organics in embryos than crusts. However,  
451 quantification of the differences in number concentration varied little among shells. The 90.5% points showed that differences  
452 in number concentration of the same kind particles in a shell compared to the previous shell at the same diameter was within  
453 twice, and the maximum differences was up to 9 times (294 data points in Fig. 9). This was because the growth of hailstones  
454 beyond the embryo stage depends on the accretion of supercooled water rather than ice crystals (Lamb and Verlinde,  
455 2011). The hailstone recorded not only insoluble particles when the embryo formed, but also insoluble particle in the hailstone  
456 growth zone throughout the hailstorm. Thus, the size distribution of particles within the whole hailstones may represent the  
457 distribution of insoluble particles in deep convection where the hailstones pass through.

Formatted

Formatted: Font: 宋体, 小五



458 **Fig-9: Size distribution of insoluble particles present in natural shells of 12 hailstones. The diameter interval on the x-axis is 2  $\mu\text{m}$ .**  
 459 **The y-axis shows the particle number concentration from  $D - 1 \mu\text{m}$  to  $D + 1 \mu\text{m}$ , represented by blue triangles, orange**  
 460 **rectangles/squares, and purple diamonds, respectively. The natural shells**  
 461 **were named/denoted alphabetically with capital letters (shell A refers to embryos, and shell B/D refers to the crust of hailstones).**  
 462 **The arrow direction indicates/illustrates the tendency of particle number concentration in this each layer with regard/compared**  
 463 **to the previous layer. Uncertainty/shading is indicated by shading. Calculations are described in detail in the supplementary information. Abbreviations (corresponding to Table 1): BJ,**  
 464 **Beijing City; GY, Guyuan City - Beijing; BS, Baise City - BaiSe; FS, Fushun City; YT, Yantai City - FuShun; GY - GuYuan; GYA,**  
 465 **Guiyang City - GuiYAng; YT - YanTai.**

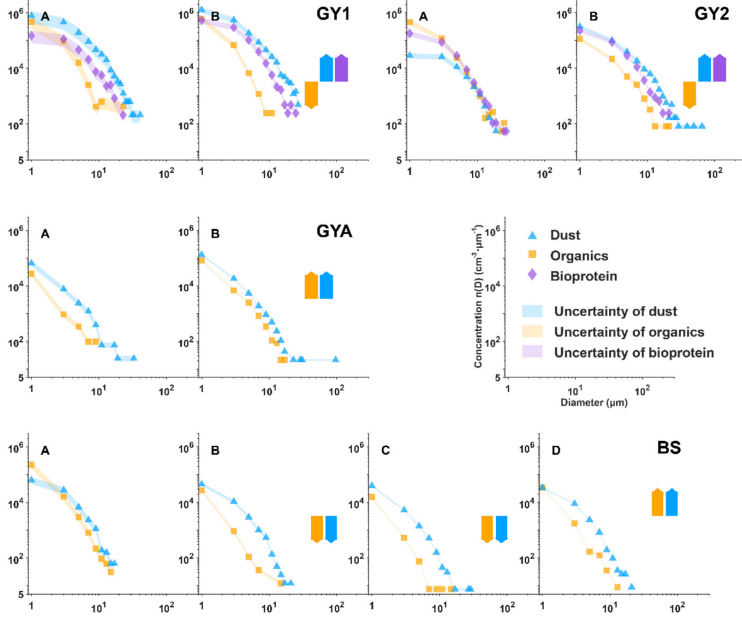


Fig. 9b is a continuation of Fig. 9a.

### 3.4 Logarithmic normal distribution of dust and organics

The size distributions of dust and organics in the whole hailstone can be described by a logarithmic normal distribution (Fig. 10a) (Lamb and Verlinde, 2011):

$$n(\ln D) = \frac{N}{\sqrt{2\pi \ln \sigma_g}} \cdot \exp \left[ -\frac{(\ln D - \ln \tau_g)^2}{2 \ln^2 \sigma_g} \right], (D > 0.2 \mu\text{m}) \quad (12)$$

$$n(\ln D) = \frac{N}{\sqrt{2\pi \ln \sigma_g}} \cdot \exp \left[ -\frac{(\ln D - \ln D_g)^2}{2 \ln^2 \sigma_g} \right], (D > 0.2 \mu\text{m}) \quad (17)$$

Where  $n(\ln D)$  is the number concentration of insoluble particles per cubic centimeter volume water ranging from  $\ln D - \frac{1}{2} \ln \sigma_g$  to  $\ln D + \frac{1}{2} \ln \sigma_g$ . Here,  $D$  represents the diameter of particles (in micrometers),  $\ln \tau_g$  is the geometric mean diameter, and  $\ln \sigma_g$  is the geometric standard deviation (Lamb and Verlinde, 2011). The number of bioprotein aerosols was below the limit of detection in some samples, so that, only the curves of organics and dust were fitted. The fitting parameters of the same species were aggregated in parameter space, and were suspected to be related to the physical properties of each species, requiring further studies for confirmation. Moreover, the fitting parameters of organics and dust particles were

Formatted: Line spacing: single, Adjust space between Latin and Asian text, Adjust space between Asian text and numbers

Formatted

Formatted: Font: 小五, Bold

Formatted: Normal, Left, Line spacing: single

483 clustered into two centroids (Fig. 10b) by the K-means method, which indicated that organics and dust have two classic modes  
484 (classic mode of organics:  $\ln r_g \ln D_o = -0.70$   ~~$\mu\text{m}$~~ ,  $\ln \sigma_o = 0.91$   ~~$\mu\text{m}$~~ , and  $N_o = 9.19 \times 10^5 \text{ cm}^{-3}$ ; classic mode of dust:  
485  $\ln r_g \ln D_d = 0.11$   ~~$\mu\text{m}$~~ ,  $\ln \sigma_d = 1.07$   ~~$\mu\text{m}$~~ , and  $N_o = 1.5859 \times 10^6 \text{ cm}^{-3}$ ). That is, insoluble organics in hailstones are usually  
486 smaller in diameter and present in lower amounts than dust. Regardless of fine or coarse particles ( $D < 0.5 \mu\text{m}$  in diameter  
487 were not considered in reference to DeMott et al. (DeMott et al., 2010)), the number concentration of dust was up to 2 orders  
488 of magnitude higher than the number concentration of organics. These observations indicated that dust accounted for the major  
489 portion of particles in eight hailstorms (no considering about bioprotein), which was consistent with the observations of  
490 embryos described above.

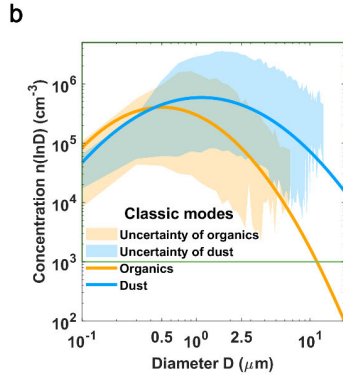
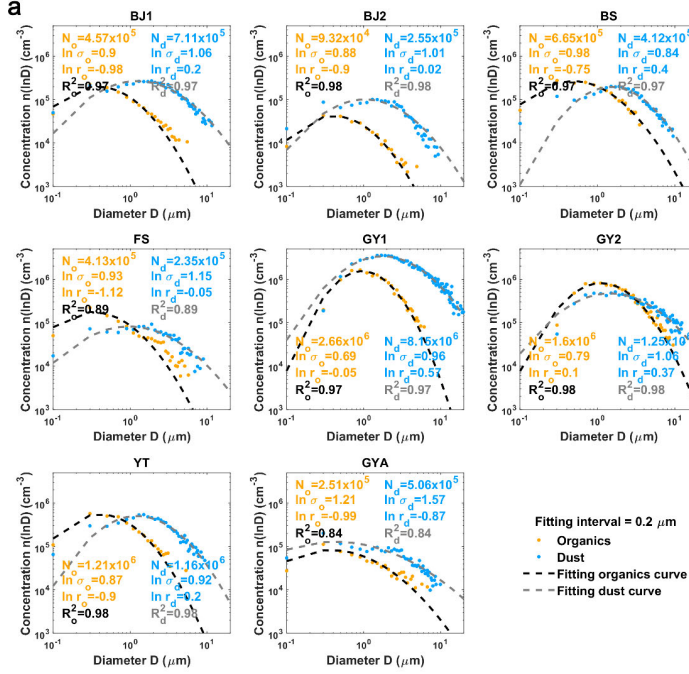
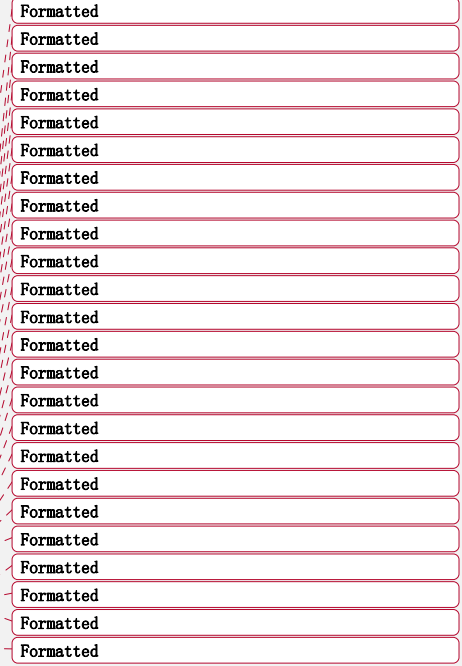


**Fig. 10:** Fitting size distribution functions of organics and dust contained in the whole hailstone. (a) Fitting parameters of logarithmic normal distributions of BJ1, BJ2, BS, FS, GY1, GY2, YT, GYA. (b) Classic modes of dust and organics (interval of data is  $0.2 \mu\text{m}$  and fitting curves painted with interval of  $0.02 \mu\text{m}$ ). The fitting range of (a) is shown with a green rectangle. The centroid of the organics fitting parameter (orange line) is  $\ln \sigma_o = 0.91 \mu\text{m}$ ,  $\ln r_o \cdot \ln D_o = -0.70 \mu\text{m}$ , and  $N_o = 9.19 \times 10^5 \text{ cm}^{-3}$ . The centroid of the dust fitting parameter (blue line) is  $\ln \sigma_d = 1.07 \mu\text{m}$ ,  $\ln r_d \cdot \ln D_d = 0.11 \mu\text{m}$ , and  $N_d = 1.59 \times 10^6 \text{ cm}^{-3}$ . Shading showed uncertainty of organics and dust. Abbreviations (corresponding to Table 1): BJ, Beijing City; GY, Guyuan City - Beijing; BS, Baise City - BaiSe; FS, Fushun City; YT, Yantai City - FuShun; GY, GuYuan; GYA, Guiyang City.





499 ~~- GuiYang; YT - YanTai~~

Formatted

500 **4 Conclusions**

501 This was the first study to simultaneously analyze both the number concentrations and species (~~organics, dust and~~  
502 ~~bioproteins~~) of insoluble particles in hailstones. Analysis of insoluble particles present in hailstones, which participate in  
503 ~~heterogeneous nucleating process as ice-nucleating particles in a deep convection~~(Lamb and Verlinde, 2011), provides a new  
504 ~~approach for refinement of particle observation in severe storms and the understanding of hailstone formation including~~  
505 ~~organics, dust and bioproteins~~) of insoluble particles in hailstones. The findings from this analysis offer valuable insights into  
506 ~~particle observations within severe storms. Understanding the number concentration and composition of these insoluble~~  
507 ~~particles is crucial, as they play a significant role as ice-nucleating particles during the heterogeneous nucleation process in~~  
508 ~~deep convection.~~

Formatted

Formatted

509 The size distribution of insoluble particles in hailstones from the same hailstorm showed less variation than those from  
510 different hailstorms. One possible reason is that updrafts of hailstorms brought insoluble particles from local surfaces or  
511 boundary layers into deep convective clouds. ~~Moreover, part of these insoluble particles participate in freezing initial ice~~  
512 ~~particles to form one type of hailstone embryos. Almost all insoluble particles in hailstone embryos analyzed in this study~~  
513 ~~showed an exponential size distribution, which was consistent with the effects of gravity. The number concentrations of~~  
514 ~~organics and dust from different hailstone embryos differed up to 389 times and 526 times at the same diameter, respectively.~~  
515 ~~Moreover, almost all insoluble particles in hailstone embryos analyzed in this study showed an exponential size distribution,~~  
516 ~~which was consistent with the effects of gravity. The number concentrations of organics and dust from different hailstone~~  
517 ~~embryos differed up to 389 times and 526 times at the same diameter, respectively. The changes in particle concentration may~~  
518 ~~lead to at least one-order-of-magnitude variance in ice-nucleating particle~~ (DeMott et al., 2010). Additionally, size distribution  
519 ~~of insoluble particles varied in shells up to 27~~Hailstone samples with high insoluble particle content, i.e., GY1 and GY2,  
520 ~~showed significantly lower total column water vapor values and smaller depth between freezing level height and orography~~  
521 ~~within one hour before hailstorm occurrence, compared to other samples~~ (Hersbach et al., 2018). The competition of  
522 ~~condensation and shorter updraft pathway might be responsible for the high number concentrations of organics, dust, and~~  
523 ~~bioproteins in GY1 and GY2. Size distribution of insoluble particles varied in shells up to 9 times, which was much smaller than~~  
524 differences with different hailstorms.

525 Two classic logarithmic normal distribution models were applied to fit the size distribution modes of organics and dust  
526 ~~within hailstones were fitted as logarithmic normal distribution for, providing a~~ description of insoluble particles in the deep  
527 ~~convection where the hailstones grew up. The~~during hailstone formation. The analysis of the two classic size distribution  
528 modes of insoluble particles ~~suggested that~~indicated a significant presence of dust-occupied the major fraction, without

Formatted

Formatted

Formatted

Formatted

Formatted

Formatted

Formatted

Formatted

Formatted

Formatted

529 ~~taking considering~~ bioprotein into account. ~~Besides, there is.~~ Furthermore, a positive correlation ~~exists~~ between the number  
530 concentrations of insoluble particles and ~~that of~~ ice-nucleating particles in hailstones, ~~specifically~~ for corresponding species  
531 (Ren et al., 2023, submitted, figure not shown). ~~Further~~A further measurement of ice-nucleating particles by drop-freezing  
532 experiments will establish the relationship between insoluble particles and ~~immersion~~ ice-nucleating particles. Combination  
533 of these results with future experiments to determine the number concentrations and species of particles from local observations  
534 will establish the relationship between surface observation and ice-nucleating particles in deep convective clouds, which will  
535 lead to improvement of the parameterization of ice-nucleating particles in both weather and climate models.

536 ~~However~~Nonetheless, two kinds of classic size distribution modes of organics and dust in hailstones were performed, but  
537 a more robust classic mode required a larger number of samples. In future, for ~~any~~ climate or weather models, the classic mode  
538 can be assumed as the mean state to describe the characteristics of insoluble particles in supercooling water. In addition, this  
539 study did not attempt to parameterize bioprotein aerosols, because there was a great uncertainty in quantification due to poor  
540 understanding of biological processes (Fröhlich-Nowoisky et al., 2016). Further collaborative studies are required to gain a  
541 better understanding of biological processes to establish the classic bioprotein mode.

#### 542 Code availability

543 Self-organized maps algorithm is functions on MATLAB  
544 <https://ww2.mathworks.cn/help/deeplearning/ref/selforgmap.html>  
545 Random forest algorithm is functions on MATLAB  
546 [https://ww2.mathworks.cn/help/stats/treebagger.html?searchHighlight=TreeBagger&s\\_tid=srchtitle\\_TreeBagger\\_1](https://ww2.mathworks.cn/help/stats/treebagger.html?searchHighlight=TreeBagger&s_tid=srchtitle_TreeBagger_1)  
547 The 10-fold stratified cross-validation algorithm is functions on MATLAB  
548 [https://ww2.mathworks.cn/help/stats/cvpartition.html?searchHighlight=cvpartition&s\\_tid=srchtitle\\_cvpartition\\_1](https://ww2.mathworks.cn/help/stats/cvpartition.html?searchHighlight=cvpartition&s_tid=srchtitle_cvpartition_1)  
549 Identification algorithms are coded on MATLAB and will be made available on request.

#### 550 Data availability

551 Data will be made available on request.

#### 552 Author contributions

553 Haifan Zhang wrote the original draft under the concept presented by Qinghong Zhang. Haifan Zhang, Xiangyu Lin and  
554 Chan-Pang Ng participated in preprocess and reservation of hailstones from volunteers. Haifan Zhang and Xiangyu Lin sliced  
555 hailstones using machine manufactured by Kai Bi and performed the experiments on analyzing element weight ratio of

Formatted  
Formatted  
Formatted  
Formatted  
Formatted

556 insoluble particles with help of Li Chen. Kai Bi also provided hailstones BJ2 ~ BJ6. Machine learning on identification of  
557 particles is operated by Haifan Zhang. Yangze Ren and Huiwen Xue compared ice nucleation particles from drop-freezing  
558 experiments with our data. Zhuolin Chang provided hailstones GY1 and GY2. All authors discussed and contributed to the  
559 final manuscript. Qinghong Zhang directed this project.

#### 560 **Competing interests**

561 The authors declare no competing interests.

#### 562 **Acknowledgments**

563 This study was supported by the National Natural Science Foundation of China (Grant Nos. 42030607 and 41930968),  
564 the Innovation Project of the China Meteorological Administration (Grant No. CXFZ2021J038) and the Key R & D projects  
565 in Ningxia Hui Autonomous Region (2022BEG02010). The authors thank Cai Yao from the Meteorological Bureau of  
566 Guangxi, China in collecting hailstones BS in Guangxi. The authors thank volunteers in collecting hailstones. The authors  
567 thank Prof. Jiwen Fan from Pacific Northwest National Laboratory of the United States for discussions.

568 **References:**

569 [Aztec User Manual:](#)

570 <https://utw10193.utweb.utexas.edu/InstrumentManuals/Oxford%20EDS%20AZtec%20User%20Manual.pdf>, last access:

571 [22 August 2023.](#)

572 ~~Ault, A. P., Peters, T. M., Sawvel, E. J., Casuccio, G. S., Willis, R. D., Norris, G. A., and Grassian, V. H.: Single-Particle-~~  
573 ~~SEM-EDX Analysis of Iron-Containing Coarse Particulate Matter in an Urban Environment: Sources and Distribution~~  
574 ~~of Iron within Cleveland, Ohio, *Environ. Sci. Technol.*, 46, 4331–4339, <https://doi.org/10.1021/es204006k>, 2012.~~

575 Battaglia, A., Mroz, K., and Cecil, D.: Satellite hail detection, in: *Precipitation Science*, Elsevier, 257–286,

576 <https://doi.org/10.1016/B978-0-12-822973-6.00006-8>, 2022.

577 Beal, A., Martins, J. A., Rudke, A. P., de Almeida, D. S., da Silva, I., Sobrinho, O. M., de Fátima Andrade, M., Tarley, C. R.

578 T., and Martins, L. D.: Chemical characterization of PM<sub>2.5</sub> from region highly impacted by hailstorms in South

579 America, *Environ. Sci. Pollut. Res.*, 29, 5840–5851, <https://doi.org/10.1007/s11356-021-15952-6>, 2022.

580 Calinski, T. and Harabasz, J.: A dendrite method for cluster analysis, *Commun. Stat. - Theory Methods*, 3, 1–27,

581 <https://doi.org/10.1080/03610927408827101>, 1974.

582 Chen, Q., Yin, Y., Jiang, H., Chu, Z., Xue, L., Shi, R., Zhang, X., and Chen, J.: The Roles of Mineral Dust as Cloud

583 Condensation Nuclei and Ice Nuclei During the Evolution of a Hail Storm, *J. Geophys. Res. Atmos.*, 124, 14262–

584 14284, <https://doi.org/10.1029/2019JD031403>, 2019.

585 Davies, D. L. and Bouldin, D. W.: A Cluster Separation Measure, *IEEE Trans. Pattern Anal. Mach. Intell.*, PAMI-1, 224–

586 227, <https://doi.org/10.1109/TPAMI.1979.4766909>, 1979.

587 DeMott, P. J., Prenni, A. J., Liu, X., Kreidenweis, S. M., Petters, M. D., Twohy, C. H., Richardson, M. S., Eidhammer, T.,

588 and Rogers, D. C.: Predicting global atmospheric ice nuclei distributions and their impacts on climate, *Proc. Natl. Acad.*

589 *Sci.*, 107, 11217–11222, <https://doi.org/10.1073/pnas.0910818107>, 2010.

590 DeMott, P. J., Prenni, A. J., McMeeking, G. R., Sullivan, R. C., Petters, M. D., Tobo, Y., Niemand, M., Möhler, O., Snider,

591 J. R., Wang, Z., and Kreidenweis, S. M.: Integrating laboratory and field data to quantify the immersion freezing ice

592 nucleation activity of mineral dust particles, *Atmos. Chem. Phys.*, 15, 393–409, <https://doi.org/10.5194/acp-15-393->

593 2015, 2015.

594 Fröhlich-Nowoisky, J., Kampf, C. J., Weber, B., Huffman, J. A., Pöhlker, C., Andreae, M. O., Lang-Yona, N., Burrows, S.

595 M., Gunthe, S. S., Elbert, W., Su, H., Hoor, P., Thines, E., Hoffmann, T., Després, V. R., and Pöschl, U.: Bioaerosols in

596 the Earth system: Climate, health, and ecosystem interactions, *Atmos. Res.*, 182, 346–376,

597 <https://doi.org/10.1016/j.atmosres.2016.07.018>, 2016.

598 Hersbach, H., Bell, B., Berrisford, P., Biavati, G., Horányi, A., Muñoz Sabater, J., Nicolas, J., Peubey, C., Radu, R., Rozum,

599 I., Schepers, D., Simmons, A., Soci, C., Dee, D., and Thépaut, J.-N.: ERA5 hourly data on single levels from 1959 to  
600 present, Copernicus Clim. Chang. Serv. Clim. Data Store (CDS).[data set],  
601 <https://doi.org/https://doi.org/10.24381/cds.adbb2d47>, 2018.

602 Hoose, C. and Möhler, O.: Heterogeneous ice nucleation on atmospheric aerosols: a review of results from laboratory  
603 experiments, *Atmos. Chem. Phys.*, 12, 9817–9854, <https://doi.org/10.5194/acp-12-9817-2012>, 2012.

604 ~~Hoose, C., Kristjánsson, J. E., Chen, J. P., and Hazra, A.: A Classical Theory Based Parameterization of Heterogeneous Ice  
605 Nucleation by Mineral Dust, Soot, and Biological Particles in a Global Climate Model, *J. Atmos. Sci.*, 67, 2483–2503,  
606 <https://doi.org/10.1175/2010JAS3425.1>, 2010.~~

607 ~~Jouzel, J., Merlivat, L., and Roth, E.: Isotopic study of hail, *J. Geophys. Res.*, 80, 5015–5030,  
608 <https://doi.org/10.1029/JC080i036p05015>, 1975.~~

609 ~~Kirpes, R. M., Bondy, A. L., Bonanno, D., Moffet, R. C., Wang, B., Laskin, A., Ault, A. P., and Pratt, K. A.: Secondary  
610 sulfate is internally mixed with sea spray aerosol and organic aerosol in the winter Arctic, *Atmos. Chem. Phys.*, 18,  
611 3937–3949, <https://doi.org/10.5194/acp-18-3937-2018>, 2018.~~

612 Knight, N. C.: The Climatology of Hailstone Embryos, *J. Appl. Meteorol.*, 20, 750–755, [https://doi.org/10.1175/1520-0450\(1981\)020<0750:TCOHE>2.0.CO;2](https://doi.org/10.1175/1520-0450(1981)020<0750:TCOHE>2.0.CO;2), 1981.

613 ~~Kohonen, T.: The self-organizing map, *Proc. IEEE*, 78, 1464–1480, <https://doi.org/10.1109/5.58325>, 1990.~~

614 Lamb, D. and Verlinde, J.: *Physics and Chemistry of Clouds*, Cambridge University Press, Cambridge,  
615 <https://doi.org/10.1017/CBO9780511976377>, 2011.

616 Li, X., Zhang, Q., Zhu, T., Li, Z., Lin, J., and Zou, T.: Water-soluble ions in hailstones in northern and southwestern China,  
617 *Sci. Bull.*, 63, 1177–1179, <https://doi.org/10.1016/j.scib.2018.07.021>, 2018.

618 Li, X., Zhang, Q., Zhou, L., and An, Y.: Chemical composition of a hailstone: evidence for tracking hailstone trajectory in  
619 deep convection, *Sci. Bull.*, 65, 1337–1339, <https://doi.org/10.1016/j.scib.2020.04.034>, 2020.

620 Michaud, A. B., Dore, J. E., Leslie, D., Lyons, W. B., Sands, D. C., and Priscu, J. C.: Biological ice nucleation initiates  
621 hailstone formation, *J. Geophys. Res. Atmos.*, 119, 12,186-12,197, <https://doi.org/10.1002/2014JD022004>, 2014.

622 Prenni, A. J., Demott, P. J., Rogers, D. C., Kreidenweis, S. M., Mcfarquhar, G. M., Zhang, G., and Poellot, M. R.: Ice nuclei  
623 characteristics from M-PACE and their relation to ice formation in clouds, *Tellus B*, 61, 436–448,  
624 <https://doi.org/10.1111/j.1600-0889.2009.00415.x>, 2009.

625 Rogers, D. C., DeMott, P. J., Kreidenweis, S. M., and Chen, Y.: A Continuous-Flow Diffusion Chamber for Airborne  
626 Measurements of Ice Nuclei, *J. Atmos. Ocean. Technol.*, 18, 725–741, [https://doi.org/10.1175/1520-0426\(2001\)018<0725:ACFDCF>2.0.CO;2](https://doi.org/10.1175/1520-0426(2001)018<0725:ACFDCF>2.0.CO;2), 2001.

627  
628  
629 Rosinski, J.: Solid Water-Insoluble Particles in Hailstones and Their Geophysical Significance, *J. Appl. Meteorol.*, 5, 481–

630 492, [https://doi.org/10.1175/1520-0450\(1966\)005<0481:SWIPIH>2.0.CO;2](https://doi.org/10.1175/1520-0450(1966)005<0481:SWIPIH>2.0.CO;2), 1966.

631 Rousseeuw, P. J.: Silhouettes: A graphical aid to the interpretation and validation of cluster analysis, *J. Comput. Appl.*  
632 *Math.*, 20, 53–65, [https://doi.org/10.1016/0377-0427\(87\)90125-7](https://doi.org/10.1016/0377-0427(87)90125-7), 1987.

633 Sibson, R. and Hartigan, J. A.: Clustering Algorithms., *Appl. Stat.*, 25, 70, <https://doi.org/10.2307/2346526>, 1976.

634 Tao, J., Zhang, L., Cao, J., and Zhang, R.: A review of current knowledge concerning PM2.5 chemical composition, aerosol  
635 optical properties and their relationships across China, *Atmos. Chem. Phys.*, 17, 9485–9518,  
636 <https://doi.org/10.5194/acp-17-9485-2017>, 2017.

637 [Taylor, J. R.: \*An Introduction to Error Analysis, Second ed.\*, University Science Books, 330 pp., 1997.](#)

638 Vali, G.: Ice Nucleation Relevant to Formation of Hail, 1968.

639 Vergara-Temprado, J., Miltenberger, A. K., Furtado, K., Grosvenor, D. P., Shipway, B. J., Hill, A. A., Wilkinson, J. M.,  
640 Field, P. R., Murray, B. J., and Carslaw, K. S.: Strong control of Southern Ocean cloud reflectivity by ice-nucleating  
641 particles, *Proc. Natl. Acad. Sci.*, 115, 2687–2692, <https://doi.org/10.1073/pnas.1721627115>, 2018.

Formatted: Font: 10 pt